Research in Astronomy and Astrophysics, 24:095016 (12pp), 2024 September https://doi.org/10.1088/1674-4527/ad4f25

A Novel Two-dimensional Low-redundancy Array Design for Solar Radio Imaging

Weidan Zhang (张卫丹)[1], Bing Wang (王冰)[1], Zhao Wu (武昭)[1], Guang Lu (路光)[1], Yao Chen (陈耀)[1,2], and Yan Fabao (严发宝)[1,3]

[1] Laboratory for Electromagnetic Detection, Institute of Space Sciences, Shandong University, Weihai 264209, China; yanfabao2022@163.com
[2] Center for Integrated Research on Space Science, Astronomy, and Physics, Institute of Frontier and Interdisciplinary Science, Shandong University, Qingdao 266237, China
[3] School of Mechanical, Electrical & Information Engineering, Shandong University, Weihai 264209, China
Received 2024 January 30; revised 2024 May 13; accepted 2024 May 21; published 2024 September 13

Abstract

The radioheliograph is an extensive array of antennas operating on the principle of aperture synthesis to produce images of the Sun. The image acquired by the telescope results from convoluting the Sun's true brightness distribution with the antenna array's directional pattern. The imaging quality of the radioheliograph is affected by a multitude of factors, with the performance of the "dirty beam" being simply one component. Other factors such as imaging methods, calibration techniques, clean algorithms, and more also play a significant influence on the resulting image quality. As the layout of the antenna array directly affects the performance of the dirty beam, the design of an appropriate antenna configuration is critical to improving the imaging quality of the radioheliograph. Based on the actual needs of observing the Sun, this work optimized the antenna array design and proposed a two-dimensional low-redundancy array. The proposed array was compared with common T-shaped arrays, Y-shaped arrays, uniformly spaced circular arrays, and three-arm spiral arrays. Through simulations and experiments, their performance in terms of sampling point numbers, UV coverage area, beam-half width, sidelobe level, and performance in the absence of antennas are compared and analyzed. It was found that each of these arrays has its advantages, but the two-dimensional low-redundancy array proposed in this paper performs best in overall evaluation. It has the shortest imaging calculation time among the array types and is highly robust when antennas are missing, making it the most suitable choice.

Key words: instrumentation: interferometers – methods: observational – techniques: interferometric

1. Introduction

A solar flare originates from the rapid release of magnetic energy in the solar corona, which can accelerate high-energy electrons and enhance electromagnetic radiation that covers almost the entire spectrum. It is the most hazardous solar eruption activity (Bastian et al. 1998). The energy release process of a solar flare originates from magnetic reconnection in the low corona flare region. Understanding a flare eruption's magnetic field structure and evolution is the core issue in solar flare physics research. According to changes in frequency, microwave bursts originate from plasma radiation, cyclotron radiation, and synchrotron radiation, carrying physical information about the magnetic field structure and high-energy electrons in the flare region (Dulk 1985). They can be used to diagnose the distribution and evolution of the magnetic field in the flare region and, the acceleration and transport of high-energy electrons. A radioheliograph is a fundamental tool for conducting regular solar radio observations, providing high spatial, temporal, and frequency resolution observations of the flare eruption region. Consequently, it has gained increasing recognition from the academic community.

The radioheliograph enables real-time solar observation through aperture synthesis imaging, with the core issue in its construction being the design of a reasonable antenna array. Unlike typical radio sources, the Sun is an extended and changing source with a large dynamic range, which requires the radioheliograph to have both high dynamic range and excellent instantaneous imaging capabilities; this places higher demands on the design of the antenna array and dynamic range for the radioheliograph. According to the principle of aperture synthesis imaging, the true brightness distribution of the radio source convolved with the dirty beam results in a dirty image. The dirty beam and the sampling function of the antenna array are Fourier transform pairs (Taylor et al. 1999). The arrangement of antenna positions determines the distribution of the sampling function (i.e., dirty beam) on the UV plane. Therefore, the configuration of the antenna array is a key factor that affects the imaging quality and speed of the dirty image. Additionally, the distribution of sampling points of all baselines formed by the antenna array on the UV plane is called the UV coverage, which has a decisive impact on the performance

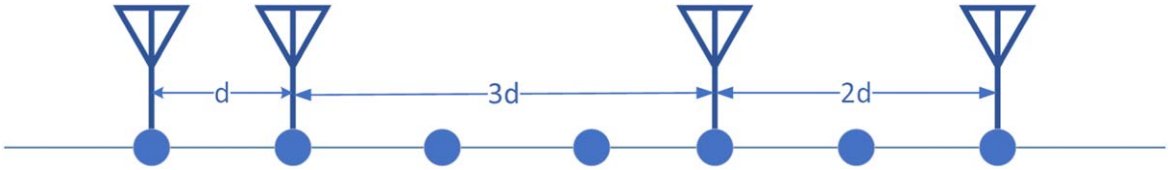

Figure 1. The minimum redundancy array with four antennas has the shortest baseline of d and the longest baseline of 6d.

of the radioheliograph. For example, short baselines are more sensitive to large-scale contours, while long baselines affect small-scale details of the radioheliograph. Therefore, high-quality radio imaging observation requires a well-designed and efficient antenna array.

The arrangement of antenna arrays requires consideration of two main aspects: the first is to ensure the quality of the signal collected by the antenna array, which includes optimizing parameters such as UV coverage, sidelobe level, and sensitivity. The second aspect is to use limited resources to avoid excessive baseline redundancy in complex calculations and to achieve high-performance imaging. Therefore, depending on the different scientific objectives and needs, the arrangement of antenna arrays often requires a compromise solution (Thompson et al. 2017).

Early radioheliographs used two arrays - the T-shaped array and the Y-shaped array. The T-type array has a simple structure and a regular rectangular UV coverage. Its imaging and calibration algorithms are relatively easy to calculate, and there is no interpolation error. As a result, it was widely used in early radioheliograph construction. For example, The Nancay Multi-frequency Radioheliograph (NRH, Condon et al. 1998), Nobeyama Radio Heliograph (NoRH. Nakajima et al. 1985), and Siberian Radioheliograph (Lesovoi et al. 2017) all used this type of array. The T-shaped array, however, has some significant problems. For example, when the number of elements is the same, this array has more baseline redundancy (greater than 50%) compared to other arrays. The equilateral Y-shaped array, on the other hand, is widely used in radioheliograph construction, such as the Very Large Array (Condon et al. 1998), because of its excellent scalability and outstanding UV coverage performance. However, this type of array also has some drawbacks. The antennas are distributed in specific directions, creating a hexagonal UV coverage pattern. As a result, the resolution is relatively low in some directions, and the imaging and calibration algorithms are more complex.

In recent years, the solar physics community has started applying several new antenna arrays, namely the three-armed spiral, circular, and Reuleaux triangle array (Keto 1997). The three-armed spiral array has received considerable attention due to its Gaussian distribution in the baseline and lack of redundancy. It can provide a more significant field of view and frequency coverage than T-shaped and Y-shaped arrays. It is used in the Mingantu spectral radioheliograph (MUSER, Yan et al. 2009) and the Expanded Owens Valley Solar Array (Perley et al. 2011). However, these distributed arrays are relatively complicated, requiring a larger surface area for the antennas. Additionally, the irregular UV coverage pattern leads to larger computational imaging requirements. Circular ring and Reuleaux triangle arrays provide the most uniform UV coverage and, under the same maximum baseline condition, have higher resolution and no redundancy. However, the uneven distribution of sampling points makes it difficult for subsequent imaging calculations, requiring a considerable amount of time to grid. Furthermore, these arrays cannot be extended or scaled. The newly built Daocheng Solar Radio Telescope (Lu et al. 2022) uses a uniform circular array.

Overall, the advantages and disadvantages of common antenna array arrangements are apparent, and it is challenging to satisfy all requirements, such as low baseline redundancy, excellent UV coverage, and fast image processing, in practical applications. Therefore, designing new arrays that balance imaging observations and calibration calculations while achieving scientific goals is crucial. This paper proposes a new two-dimensional low-redundancy array design that effectively resolves the conflict between the number of antennas and computational requirements. This design simultaneously reduces imaging computational costs while providing high-quality imaging. The second section introduces the calculations involved in the two-dimensional low-redundancy array. The third section conducts simulation analyzes of commonly used arrays and the minimum redundancy array for imaging performance. The fourth section summarizes the entire paper.

2. Two-dimensional Low-redundancy Array

Optimizing antenna array design is to achieve sufficient, uniform, low-redundancy UV coverage using as few antenna elements as possible. This approach enables relatively high spatial resolution by designing a minimum redundancy linear array (MRLA. Moffet 1968). As shown in Figure 1, the MRLA can be represented as {0, 1, 4, 6}. It comprises only four antennas, yet its baseline length is equivalent to a uniform linear array with six antennas.

For a one-dimensional linear array, the definition of redundancy is (Ishiguro 1980):

$$R = \frac{C_n^2}{L}, \tag{1}$$

where C_n^2 represents the permutation and combination of array elements, n represents the number of array elements, and L represents the longest continuous baseline. Leech (1956) indicated that for $n \leqslant 11$, the optimal redundancy range of MRLA is $1.217 \leqslant R \leqslant 1.332$. When $n > 11$, the resulting redundancy of the antenna array would be insufficient to reach within that range, thus denoting the array as a low-redundancy linear array (LRLA, Ruf 1993). An LRLA is widely used in the radar field. Many algorithms have been developed specifically for obtaining an LRLA, including the cyclic difference, simulated annealing algorithm, particle swarm algorithm, and others (Lee & Pillai 1988; Ruf 1993; Camps et al. 2001).

An LRLA can comprehensively cover all possible baseline lengths within a maximum baseline interval. A two-dimensional low-redundancy array can be constructed by "multiplying" any two LRLAs, providing full coverage of a rectangular area on the UV plane and enabling two-dimensional radio imaging. This array ensures the completeness of UV coverage and achieves higher spatial resolution by obtaining a relatively large number of sampling points and UV coverage areas. In this paper, we implement this array in the following manner:

(1) Construct an LRLA arrangement a_i with n_1 antennas and the longest baseline L_1 in the x-axis direction, where $i = 1, 2, \ldots, n_1$, s is the spacing of any two antennas in a_i, such that $s \in [0, L_1]$ and can cover all possible array element spacings.

(2) Construct an LRLA arrangement b_j with n_2 antennas and the longest baseline L_2 in the$y$-axis direction, where $j = 1, 2, \ldots, n_2$, s is the spacing of any two antennas in b_j, such that $s \in [0, L_2]$ and can cover all possible array element spacings.

(3) After forming the two matrices, we perform a cartesian product to obtain a two-dimensional matrix, denoted by (a_i, b_j), where each row represents an antenna's position along the x-axis, and each column represents the position of an antenna along the y-axis. This matrix is the desired low-redundancy array that contains $n_1 \times n_2$ array elements, each antenna's position marked as (a_i, b_j). Figure 2(c) shows the 7×7 arrangement of the resulting two-dimensional low-redundancy array.

The array is characterized by redundancy and no voids in UV coverage. Such an array enhances both the strength of the signal and the reliability of the system because the redundant baseline takes multiple measurements of the same point, which can be combined to improve the signal-to-noise ratio of the signal. In addition, even if some antennas fail, the array can still obtain information about that point from other antennas. The UV coverage without nulls allows for more complete sampling and avoids problems such as aliasing during interpolation (Meurisse & Delmas 2001).

Assuming x_i represents the LRLA arrangement of n_1 elements on the x-axis, where $i = 0, 1, \ldots, n_1 - 1$, and d is the minimum distance between the elements along the axis. In contrast, y_j represents the LRLA arrangement of n_2 elements on the y-axis, where $j = 0, 1, \ldots, n_2 - 1$, and d is the minimum distance between the elements along the axis. The total number of elements in the resulting two-dimensional low-redundancy array is $n_1 \times n_2$. If the positions of any two antenna elements in the two-dimensional low-redundancy array are (x_{i_0}, y_{j_0}) and (x_{i_1}, y_{j_1}), then their corresponding spatial frequency sampling points in the (u, v) plane are given by:

$$u_{ij} = \frac{x_{i0} - x_{i1}}{\lambda} = (a_{i1} - a_{i0}) \cdot \frac{d}{\lambda}, \tag{2}$$

$$v_{ij} = \frac{y_{j0} - y_{j1}}{\lambda} = (b_{j1} - b_{j0}) \cdot \frac{d}{\lambda}. \tag{3}$$

Since $|a_{i_1} - a_{i_0}|$ can cover any integer in the interval $[0, L_1]$, the set $\{a_{i_1} - a_{i_0} | 1 \leqslant i_0, i_1 \leqslant n_1\}$ can cover any integer in the interval $[-L_1, L_1]$. Similarly, the set $\{b_{i_1} - b_{i_0} | 1 \leqslant j_0, j_1 \leqslant n_2\}$ can cover any integer in the interval $[-L_2, L_2]$. Therefore, the set $\{(a_{i_1} - a_{i_0}, b_{i_1} - b_{i_0})\}$ can cover any integer in the region $([-L_1, L_1], [-L_2, L_2])$. To clarify, the sampling area of the two-dimensional low-redundancy array on the (u, v) plane is a rectangle $([-L_1 \cdot d/\lambda, L_1 \cdot d/\lambda], [-L_2 \cdot d/\lambda, L_2 \cdot d/\lambda])$, and it provides no voids in the UV coverage, thereby eliminating any unsampled "blank areas."

3. Comparison and Analysis of Antenna Arrays

We have created a Python program to simulate and test the performance of the two-dimensional low-redundancy array. For easy comparison, we simultaneously calculated the parameters of various array types, such as T-shaped, Y-shaped, circular, and spiral arrays. During the calculation process, the shortest baseline of each array was the same, with 49 antennas. The layout, UV coverage, baseline histogram, and beam sidelobe level of each array are shown in Figures 2–5. To conduct quantitative analysis, we compared several array types from several aspects including the longest baseline, sampling point number, UV coverage area, the full width at half maxima (FWHM) of beam and sidelobe level, and the results are listed in Table 1.

The number of sampling points refers to the number of UV sampling points obtained by the antenna array. For an array of N antenna units, the number of baselines is $N(N-1)/2$ without redundancy, and $N(N-1)$ sampling points are obtained due to their conjugate symmetry. When the number of antenna elements is constant, more sampling points indicate a lower redundancy in the antennas and produce more sampling data, which can improve image reconstruction. Regarding the sampling points, we observe that the circular and spiral arrays have the highest number of sampling points, with 2352 and 2256, respectively, and both of them have no redundant baselines. The Y-shaped array has 1632 sampling points. The T-shaped array and the two-dimensional low-redundancy array have relatively fewer sampling points, with 1120 and 1224, respectively.

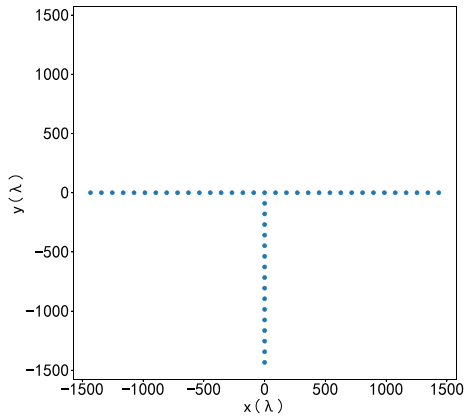

(a) T array

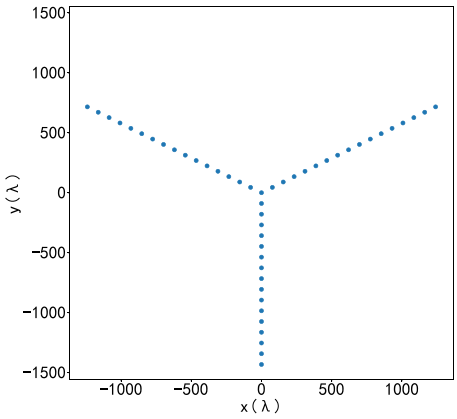

(b) Y array

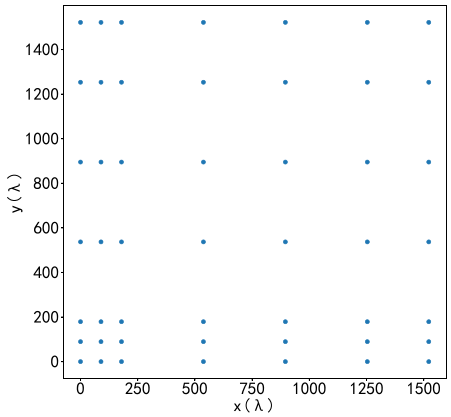

(c) Two-dimensional Low redundancy array

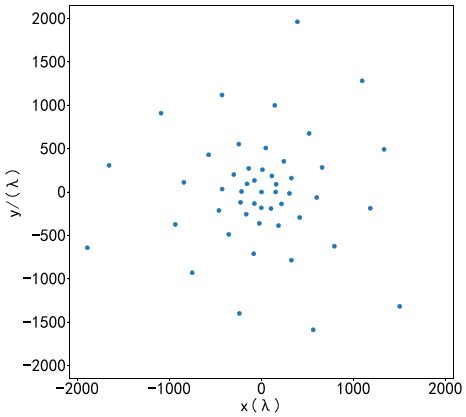

(d) Spiral array

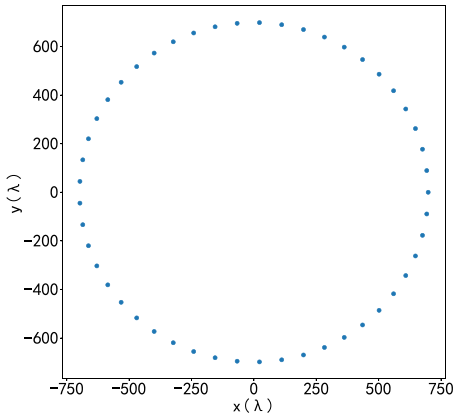

(e) Circle array

Figure 2. The array layout of the antenna arrays, with 49 array elements and the same number of the shortest baselines.

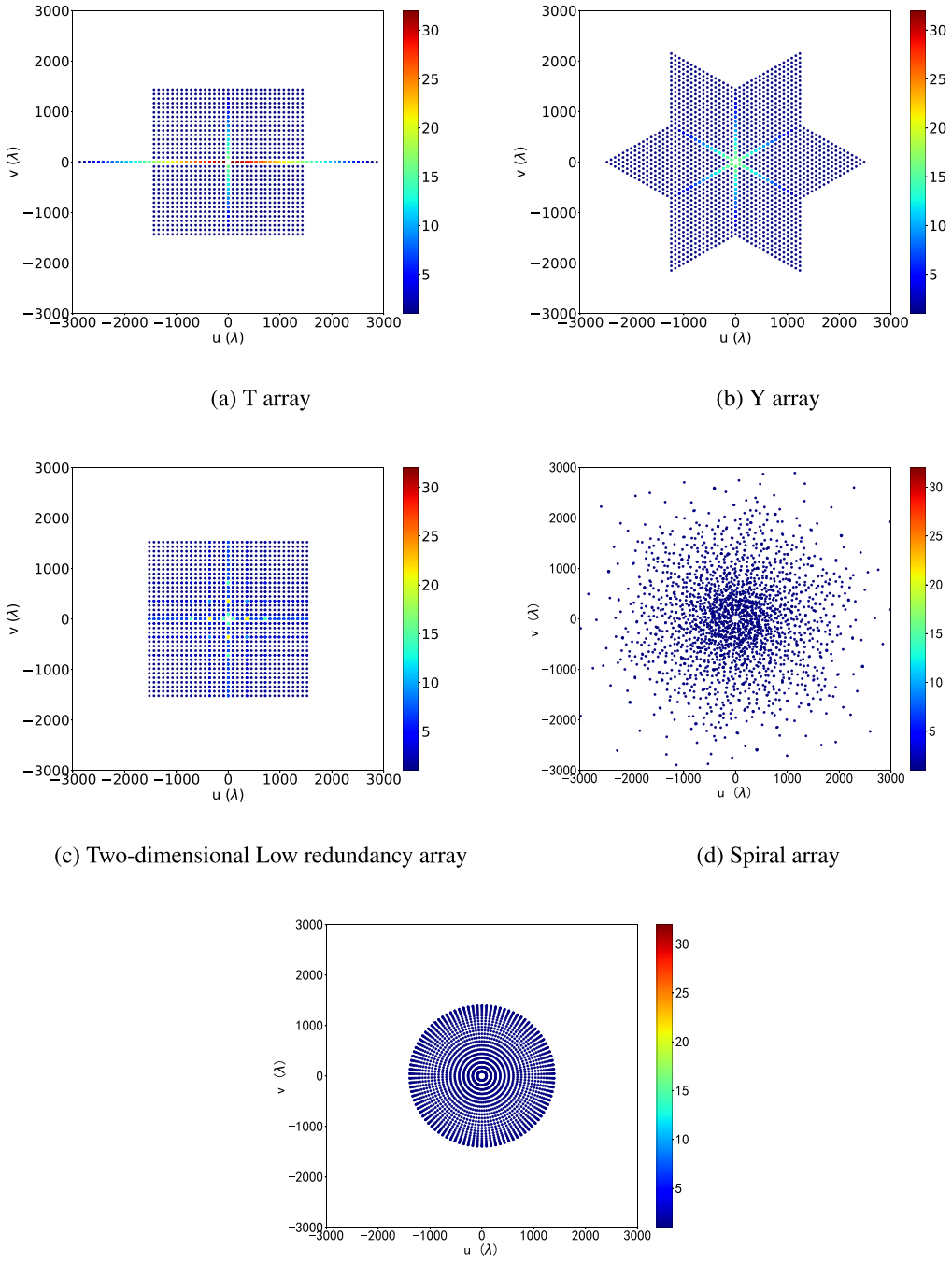

(a) T array

(b) Y array

(c) Two-dimensional Low redundancy array

(d) Spiral array

(e) Circle array

Figure 3. The comparison of UV coverage of several types of arrays.

Radio interferometry arrays typically have multiple baselines, each with varying lengths and directions, offering different orientations and resolutions. More detailed celestial images can be obtained by combining signals from different baselines. In radio astronomy observations, the choice of baseline length depends on the scale of the studied celestial object and the scientific objectives. Longer baselines are employed for high-resolution observations, particularly crucial for GHz-range radioheliographs, which are mainly focused on solar disk features. Hence, a higher resolution is desired. It

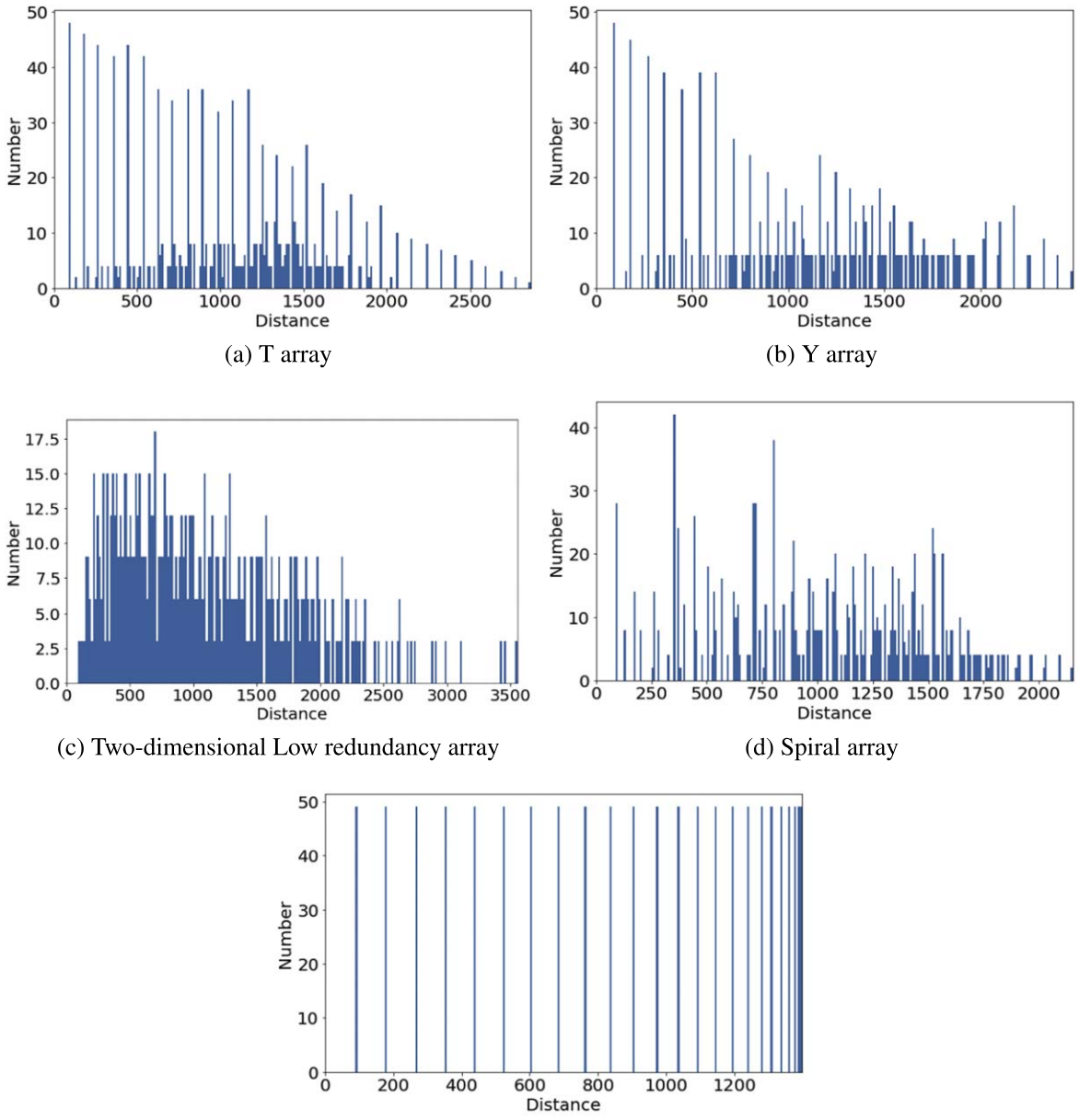

(a) T array

(b) Y array

(c) Two-dimensional Low redundancy array

(d) Spiral array

(e) Circle array

Figure 4. The baseline distribution of several types of arrays.

should be noted that, to compare the actual resolution of the heliograph, the longest baseline calculated for the T-shaped array here is the longest baseline involved in the mapping calculation, not the longest baseline in the actual position of the array. Through a comparison of the longest baselines among several arrays, it can be inferred that the Spiral array exhibits the greatest baseline length, followed by the Y-shaped array and the two-dimensional low-redundancy array.

The UV coverage area refers to the UV sampling distribution that all baselines of the antenna array form in the UV plane. Similar to the number of sampling points, the UV coverage area is also a vital parameter that characterizes the UV coverage quality of an antenna array, which affects imaging quality. UV coverage area in this context specifically denotes the distribution of UV sampling points across all baselines of the antenna array within the UV plane. It is crucial to emphasize that the UV coverage area does not correspond to a physical "area" but represents the spatial sampling distribution. In snapshot mode, the larger the UV coverage area, which means more sampling points, the better the imaging effect. In addition, when

Table 1
Comparison of Five Array Types

Antenna Array	Longest Baseline (λ)	Sampling Points Number	UV Coverage Area (%)	FWHM of the Beam (arcsec × arcsec)	Sidelobe Level (%)
T-shaped Array	1521	1120	43.4	36 × 36	13.5
Y-shaped Array	2480	1632	59.32	36 × 36	12.8
Two-dimensional 2D Low-redundancy Array	2152	1224	47.26	36 × 36	11.3
Spiral Array	3555	2256	41.31	24 × 24	6.4
Circle Array	1396	2352	34.32	72 × 72	5.8

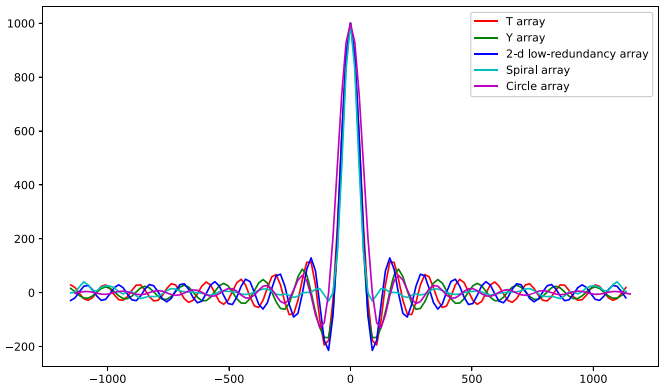

Figure 5. The profile of the beams of several types of arrays.

mapping, to apply fast Fourier transform (FFT), we want the sampling points to be located on a regular grid, and when the sampling points are irregular, gridding is needed. From Figure 3, it can be seen that the UV coverage of the T, two-dimensional low redundancy array is regular. The Y-shaped array performs best regarding the same number of elements, with an effective UV coverage area of 59.32% among the tested arrays. The two-dimensional low-redundancy array and the T-shaped array follow, demonstrating percentages of 47.26% and 43.4%, respectively. The UV coverage area of the other arrays ranges between 41.32% and 34.32%.

A radio telescope beam's FWHM is critical in determining the system resolution. As the FWHM shrinks, the system resolution improves. Effective hardware configurations are necessary to minimize the half-power width, and simulation tests have demonstrated that the spiral array provides the best resolution with an FWHM of $24'' \times 24''$. In contrast, the half-power width of the T-shaped, Y-shaped, and two-dimensional redundant array is approximately $36'' \times 36''$. The circular array provides the poorest FWHM, measuring $72'' \times 72''$.

The performance of an antenna array can be evaluated through its sidelobe level, which represents the signal strength received in directions other than its directivity. In the context of radioheliograph, the sidelobe level primarily reflects the undesirable effects of a dirty beam on the resulting dirty map. A lower sidelobe level indicates a reduced presence of false information in the dirty beam, resulting in a cleaner dirty map that is easier to recover. Based on the accompanying charts, it is evident that the spiral array exhibits the lowest sidelobe level, followed by the circular array, two-dimensional low-redundancy array, T-shaped array, and Y-shaped array.

The above analysis demonstrates that no single antenna array can achieve optimal performance across all indicators. In practical scientific applications, it is therefore crucial to carefully consider the performance parameters of an antenna layout and select the most suitable scheme based on specific requirements. For example, for the demand of high-precision imaging, antenna configurations with long baselines may be required; for large angular scale observations, antenna configurations with shorter baselines may be needed (Kale 2017). While the antenna array mentioned above presents its advantages and disadvantages, none can achieve optimal performance across all four indicators. The spiral array exhibits relatively good comprehensive performance, but its high-frequency observations suffer from an abundance of short baselines and a lack of long baselines. Moreover, despite its higher number of sampling points, the spiral array presents a limitation in its UV coverage area, leading to poor image quality. Similarly, the Y-shaped and two-dimensional low-redundancy array exhibit relatively good overall performance. Still, a thorough examination of their performance is necessary, particularly concerning image quality, a crucial factor in radioheliographs.

4. The Influence of Array Configuration on Imaging

We subsequently carried out imaging simulations of the above array to study the influence of the array on image inversion and discussed the impact of antenna absence on imaging. To better understand the influence of the array, we conducted an in-depth study on its imaging.

4.1. Imaging with Different Array Configurations

In the simulation experiment, the antenna number of each array was fixed at 49. For solar observation, the field of view should be larger than one solar radius, i.e., the field of view

should be larger than 1.2 Rsun (1152″), and the corresponding minimum baseline should be less than 107.4λ.

In the course of the imaging simulation, conventional imaging methodologies were implemented. More precisely, we sampled the sky model (shown in Figure 6(a)) using different array configurations to obtain visibilities. Following this, a direct Fourier transform was applied to the visibility function, on the principles of aperture synthesis imaging, resulting in the creation of a dirty image. To better assess the impact of the array configuration on imaging, we opted for natural weighting, with no tapering applied, and chose not to utilize the CLEAN algorithm.

Weighting amounts to giving more or less weight to certain visibilities, based on their location in the UV plane. Emphasizing long-baseline visibilities improves the image's resolution, whereas emphasizing shorter baselines improves the surface brightness sensitivity. Tapering refers to smoothing the edges of the image by reducing the weight of visibilities at large distances from the center of the image. To better reflect the effect of the formation on imaging, natural weighting, and no tapering were preferred in this paper for the imaging simulation. To comprehensively analyze the array's impact on imaging, we evaluated the imaging performance of various configurations by assessing the standard deviation of the profile residual, Root Mean Square (rms) of the Point-Spread Function (PSF) away from the 90% central peak, dynamic range and average computation time of imaging.

To calculate the standard deviation of the profile residual, we selected a slice that passed through two bright sources in the image and a profile at the same position as the sky model. The standard deviation measures the difference between the sky model and dirty maps. Figure 7 illustrates the slice profiles of the dirty map compared to the sky model. The "rms of PSF away from the 90% central peak" refers to the rms of PSF values at positions or distances away from the 90% central peak of the PSF. This measurement can be useful in characterizing the performance of an imaging system, as it tells you how much the point source's light spreads out as you move away from its central position. A smaller rms value indicates a more focused and narrower PSF, while a larger one suggests a less focused PSF. The dynamic range of an image is a key metric that quantifies the spread or range of intensities within the image. It is often used to assess the quality and contrast of an image. Here the dynamic range is defined as the ratio of the peak intensity to the absolute value of the deepest minima in the image. In this study, we have compared the computation time of imaging by measuring the computation time from visibility to the dirty map. We have conducted 100 tests to ensure accuracy and to take the average value.

Figure 6 depicts the snapshot of various array configurations for the sky model, as shown in (b)–(f). These figures reveal that several configurations can achieve relatively good imaging results for the sky model. Notably, the Y-shaped array and two-dimensional low-redundancy array exhibit good imaging effects, enabling better reflection of image details. Conversely, the three-arm spiral array presents relatively poor imaging results; this is attributed to the fact that, under fixed minimum baseline conditions and fixed observations angular scales, the spiral array's longest baseline is the longest among the various configurations. However, the array has relatively shorter baselines, which translates to a reduced level of image clarity compared to other configurations.

Table 2 compares the imaging parameters for the different array configurations. Analysis of the table reveals that the Y-shaped array has the lowest standard deviation of 13,778, followed closely by the two-dimensional low-redundancy array with 13,963, while the spiral array has the largest standard deviation of 16,445. The spiral and circle arrays exhibit the lowest rms, with values of 7.4 and 6.02 respectively. The highest dynamic range value is also the Y-shaped array at 12.26, followed by the T-shaped array, the two-dimensional low-redundancy array is next at 9.08, 8.05, and the smallest is the spiral array at 6.03.

In this study, we have compared the computation time of imaging by counting the computation time of visibility to the dirty map. We have tested it 100 times here for accuracy and took the average value. The two-dimensional low-redundancy and Y-shaped array provide the fastest computation time from visibility data to dirty images, taking 2.3 s and 2.5 s, respectively. On the other hand, the Y-shaped array and spiral array require the longest computation time, taking 3.7 s and 3.9 s, respectively.

Currently, the application of GPUs in imaging processes has revolutionized the efficiency and quality of data processing. Notably, cuGridder stands out as a GPU-based CUDA C program that significantly accelerates radio interferometric imaging by parallelizing key workflow steps, resulting in superior performance compared to traditional CPU and GPU libraries (Liu et al. 2022). Furthermore, the implementation of a high-performance imaging pipeline for MUSER data processing harnesses GPU technology to meet the massive observational data processing requirements of MUSER, enhancing both processing speed and image quality (Mei et al. 2018). Additionally, advancements such as Hybrid Gridding and Convolution-Based FFT Pruning (Muscat 2021) illustrate innovative modifications to existing techniques, demonstrating substantial acceleration in radio interferometric image synthesis while maintaining high output quality, thus highlighting the key role of GPU technology in advancing radio astronomy imaging capabilities.

4.2. The Influence of Antenna Shortage on Imaging

Assessing the impact of antenna shortages on image inversion can reveal the overall stability of antenna array operation. Given that antenna damage or malfunction is

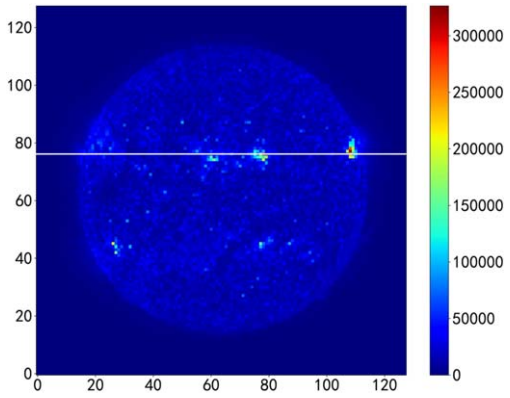

(a) Skymodel

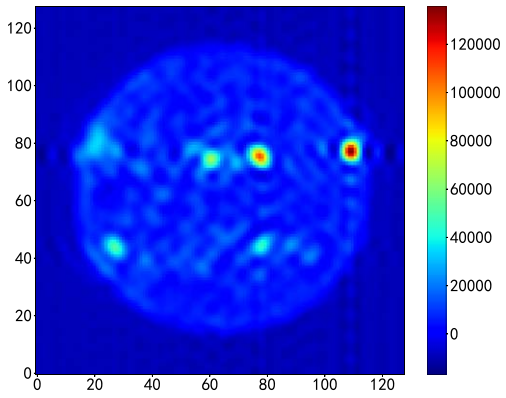

(b) T array

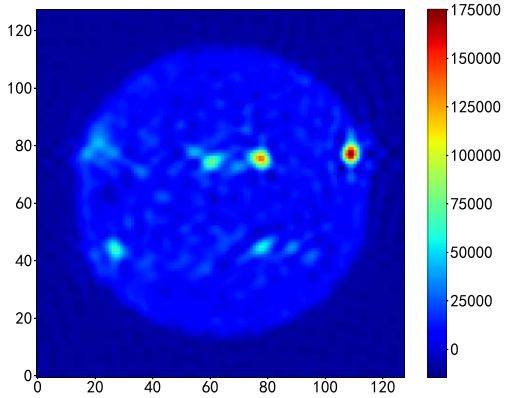

(c) Y array

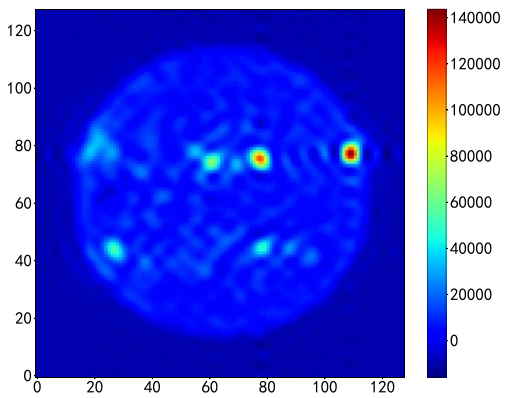

(d) Two-dimensional Low redundancy array

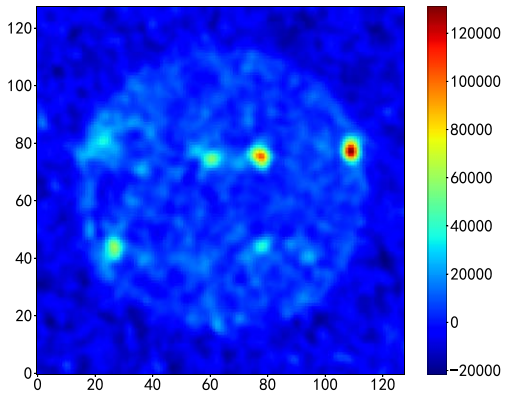

(e) Spiral array

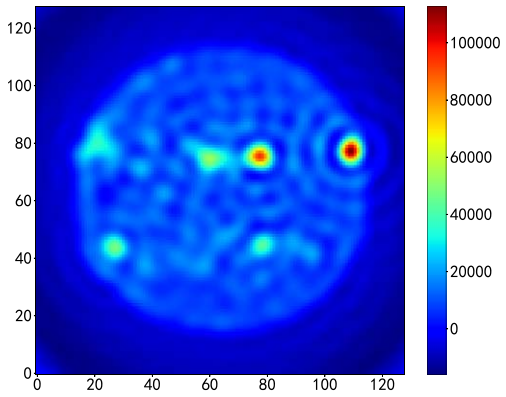

(f) Circle array

Figure 6. Different array configurations with inversion imaging results (snapshot) and the selected sky model are shown.

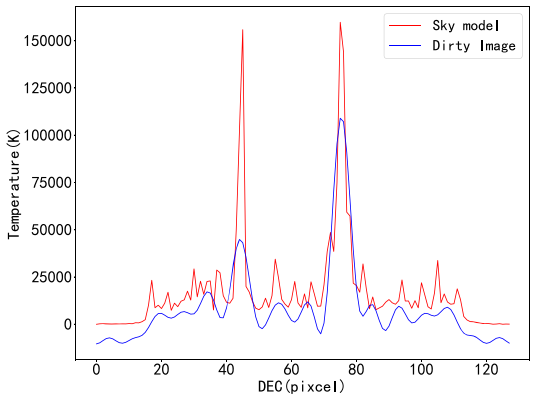

(a) T array

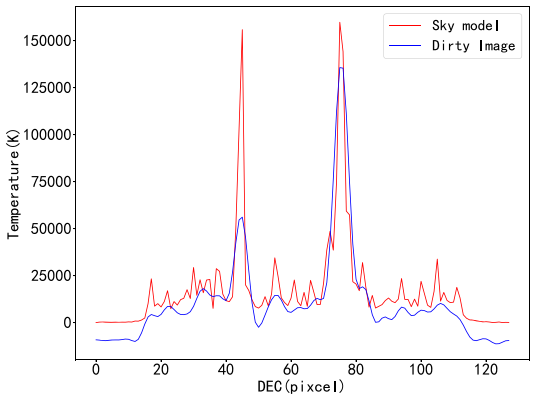

(b) Y array

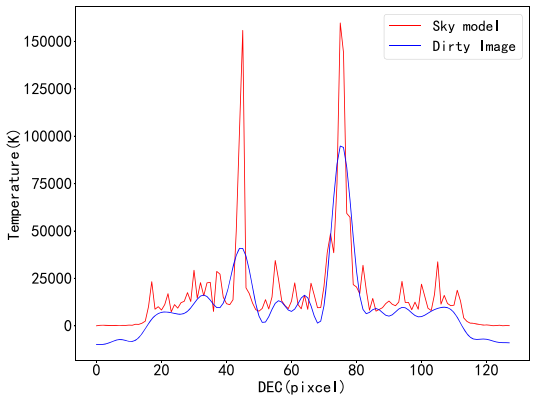

(c) Two-dimensional Low redundancy array

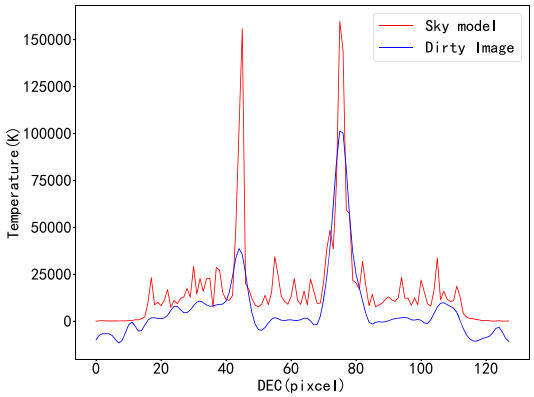

(d) Spiral array

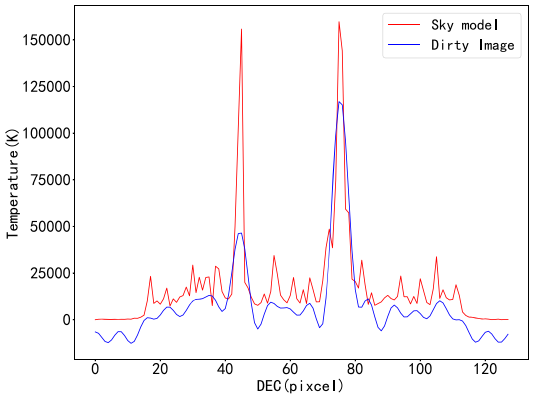

(e) Circle array

Figure 7. The profile of the sky model and the dirty map of several types of arrays.

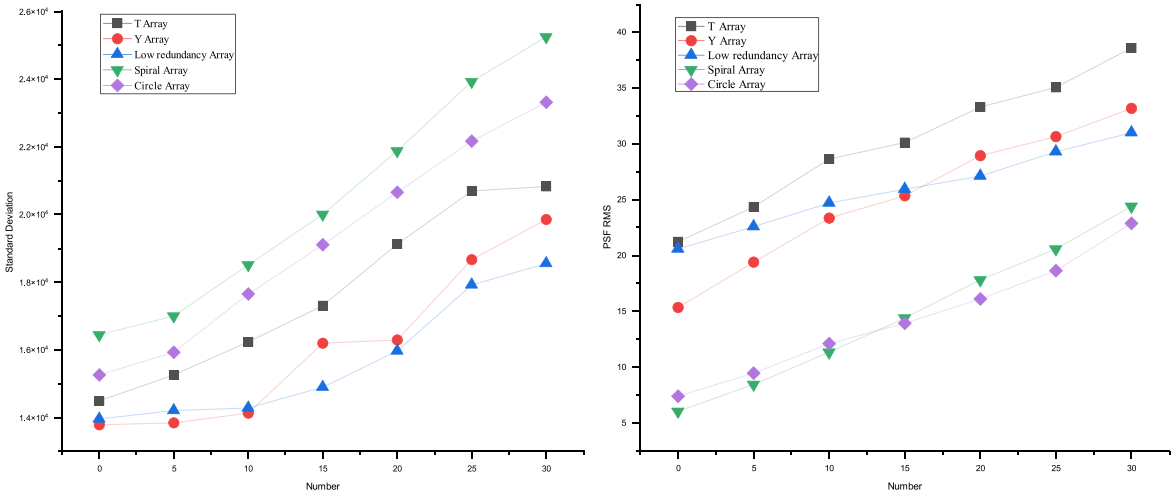

(a) The residual standard deviation of the profiles (b) PSF RMS

Figure 8. Effect of missing number of antennas on imaging.

Table 2
Comparison of Imaging Parameters for Five Array Configurations

Antenna Array	Standard Deviation	PSF rms (90%)	Dynamic Range	Calculation Time (s)
T-shaped Array	14486	21.26	8.05	2.5
Y-shaped Array	13778	15.34	12.26	3.9
two-dimensional Low-redundancy Array	13963	20.59	9.08	2.3
Spiral Array	16445	6.02	6.03	3.7
Circle aArray	15253	7.40	7.03	3.3

inevitable during telescope usage, missing one antenna will inevitably result in the loss of $N-1$ sampling points, with corresponding holes in UV coverage that negatively impact imaging. A significant number of missing antennas can severely impact imaging quality.

Given the unpredictable nature of antenna damage or malfunction during routine observation, we employed a random selection method to repeat the experiment without 1–30 antennas, for 100 repetitions, leading to 3000 experiments for analysis. In this study, we focus on comparing the residual standard deviation of the profiles and PSF rms, the corresponding change curves are shown in Figure 8.

In both figures, The two-dimensional redundant array does not have the best performance, but its robustness is the strongest as the number of missing antennas increases. This is to say that antenna absence has less effect on two-dimensional low redundancy arrays than other arrays. These findings suggest that the influence of antenna loss on the two-dimensional redundant array is relatively small. We believe this is because the baseline number of the two-dimensional low-redundancy array is relatively evenly distributed, and the redundancy of each sampling point is similar, so errors are well suppressed. When the number of elements is not large, the two-dimensional low-redundancy array has strong robustness and is more suitable.

5. Conclusion

The placement of antennas plays a critical role in determining the distribution of the complex visibility points on the UV plane, and thus, optimizing the design of the antenna array equates to optimizing the distribution of these points on the UV plane. The distribution of UV points directly affects essential parameters such as the sidelobe distribution, size, and beamwidth of the dirty beam, making optimizing the antenna array crucial in ensuring the quality of the resulting radio images. Consequently, antenna array design optimization is essential for achieving high sensitivity and resolution solar images within the desired frequency band. Generally, regular antenna configurations are used in radioheliograph array design to improve image quality.

This study comprehensively considers various factors, including baseline redundancy, UV coverage, and comprehensive aperture processing speed, to improve imaging quality and real-time imaging speed. It proposes and designs a two-dimensional low-redundancy antenna array. The antenna array is then compared and analyzed with common types, such as T-shaped array, Y-shaped array, uniform circular array, and three-arm spiral array. The following are the specific results obtained from the comparison and analysis.

(1) The UV coverage area of the two-dimensional low-redundancy antenna array is merely 12.26% smaller than that of the Y-shaped array, which has the maximum coverage area. Moreover, it is 5.85% larger than the spiral array. In all array configurations, parameters such as sampling points, beamwidth, and sidelobe level were moderate.

(2) The two-dimensional low-redundancy antenna array has an advantage in calculation time when used in imaging simulation. The standard deviation of the profile residuals is similar to that of the Y-shaped array, as is the dynamic range. This means that the imaging quality is second only to that of the Y-shaped array.

(3) The two-dimensional low-redundancy antenna array exhibits good stability. The two-dimensional low-redundancy antenna array exhibits a lower standard deviation than other array configurations. Due to its relatively even distribution of baseline numbers and similar redundancy at each sampling point, the effects of antenna failure on the two-dimensional low-redundancy array are minor, and errors can be effectively suppressed.

(4) However, the rms of a two-dimensional low redundancy array is notably large, indicating higher sidelobe levels. These elevated sidelobe levels, in turn, present challenges during the deconvolution process. These challenges arise due to the computational demands and the risk of divergence introduced by the higher sidelobes. Addressing these challenges in practice may involve implementing more complex deconvolution algorithms and utilizing advanced mathematical and computational techniques to ensure lower sidelobe levels and achieve more accurate scientific outcomes (Kogan 2000).

In summary, the two-dimensional low-redundancy antenna array is desirable due to its strong robustness and high imaging quality when the number of array elements is low. For radioheliographs that strive for high-resolution imaging, fully dense UV coverage is not achievable due to limited antenna numbers. Hence, investigating the arrangement of the antenna array for achieving satisfactory UV coverage is of great significance. In future studies, we will further explore the causes and correction methods of position errors in the antenna array, investigate the effects of positioning errors on the radioheliograph, and consider the correction methods to further enhance the performance of the radioheliograph.

Acknowledgments

This research is supported by the grants of the National Natural Science Foundation of China (42127804, 42374219).

References

Bastian, T. S., Benz, A. O., & Gary, D. E. 1998, ARA&A, 36, 131
Camps, A., Cardama, A., & Infantes, D. 2001, ITAP, 49, 1881
Condon, J. J., Cotton, W. D., Greisen, E. W., et al. 1998, AJ, 115, 1693
Dulk, G. A. 1985, ARA&A, 23, 169
Ishiguro, M. 1980, RaSc, 15, 1163
Kale, R. 2017, in 2017 32nd General Assembly and Scientific Symp. of the Int. Union of Radio Science (URSI GASS), 1
Keto, E. 1997, ApJ., 475, 843
Kogan, L. 2000, ITAP, 48, 1075
Lee, Y., & Pillai, S. 1988, in Int. Conf. on Acoustics, Speech, and Signal Processing (Piscataway, NJ: IEEE), 2674
Leech, J. 1956, JLMS, s1-31, 160
Lesovoi, S., Altyntsev, A., Kochanov, A., et al. 2017, STP, 3, 3
Liu, H., Luo, Q., & Wang, F. 2022, in 2022 IEEE 18th Int. Conf. on e-Science (e-Science) (Piscataway, NJ: IEEE), 95
Lu, G., Wang, B., Chen, Y., et al. 2022, ChJSS, 42, 294
Mei, Y., Wang, F., Wang, W., et al. 2018, PASP, 130, 014503
Meurisse, Y., & Delmas, J.-P. 2001, ITIT, 47, 464
Moffet, A. 1968, ITAP, 16, 172
Muscat, D. 2021, arXiv:2111.04141
Nakajima, H., Sekiguchi, H., Sawa, M., Kai, K., & Kawashima, S. 1985, PASJ, 37, 163
Perley, R. A., Chandler, C. J., Butler, B. J., & Wrobel, J. M. 2011, ApJ, 739, L1
Ruf, C. 1993, ITAP, 41, 85
Taylor, G. B., Carilli, C. L., & Perley, R. A. 1999, in ASP Conf. Ser. 180, Synthesis Imaging in Radio Astronomy II (San Francisco, CA: ASP)
Thompson, A. R., Moran, J. M., & Swenson, G. W. J. 2017, Interferometry and Synthesis in Radio Astronomy (3rd ed.; Berlin: Springer)
Yan, Y., Zhang, J., Wang, W., et al. 2009, EM&P, 104, 97